CHAPTER IV

S140-IRS1

4.1 Literature Reviews

The star-forming region, S140 IRS, is located in the molecular cloud L1204 at a distance of 764±27 pc (Hirota et al., 2008). In this region, there is a group of at least three ZAMS B stars (IRS 1, IRS 2, IRS 3; Beichman et al. 1979), with a total luminosity of $\sim 3 \times 10^3 \approx L_{\odot}$ (Lester et al., 1986), with IRS 1 being the brightest one at the both infrared and radio continuum wavelengths. In addition, Trinidad et al. (2007) observed IRS 1 (hereafter is IRS 1A) at all wavelengths (0.7, 1.2, 2, 3.5, and 6 cm) and also detected four new continuum peaks (IRS 1B, 1C, 1D and 1E as shown in Figure 4.1). A CO bipolar outflow extended along the northwest-southeast direction has been observed in the region by Hayashi et al. (1987). Minchin et al. (1993) found that the blue and red-shifted lobes of the CO bipolar outflow have position angles of $\sim 160°$ and $\sim 340°$, respectively. On the other hand, K band (2.0-2.3 μm) and H_2 observations have revealed two bipolar outflows in the region (Preibisch and Smith, 2002; ; Weigelt et al. 2002), one of them with an orientation similar to the CO outflow (160/340°) and the other one in the 20/200° direction. Both bipolar outflows seem to be centered on IRS 1. The region S140 IRS has also been studied at the infrared and optical bands (Eiroa et al., 1993), NH_3 lines (Verdes et al. 1989), and radio continuum emission (Schwartz, 1989; Evans et al., 1989). Hoare (2006) has observed IRS 1 at 6 cm during three epochs with MERLIN, and shows, through a very detailed analysis that it is highly elongated in the northeast-southwest direction, and also proposes that the radio continuum traces an ionized equatorial wind driven by radiation pressure from the central star and oriented in the northeast-southwest direction, perpendicular to the CO bipolar outflow.

In addition, water maser emission has also been detected toward the S140 IRS region (Tofani et al. 1995 Lekht et al., 1993; Lekht and Sorochenko, 2001; Trinidad et al. 2003). The most detailed observations are from Lekht et al. (1993) and Lekht and Sorochenko (2001), they have observed water masers during 18 years (from 1981 to 1999) with a single antenna. They obtained a spectrum of three maser features; the central component has a velocity close to that of the molecular cloud, and the lateral ones are red-shifted and blue-shifted, respectively. The anticorrelation observed between the central feature and the lateral ones was interpreted as a Keplerian disc in S140 IRS. On the other hand, Valdettaro et al. (2002) have observed water masers in this region from 1987 to 1999 with the 32 m Medicina antenna, but they did not confirm the results found by Lekht et al. (1993) and Lekht and Sorochenko (2001). In Figure 4.2, Trinidad et al. (2003) observed this source in May 1999 and from January to May 2001, they found that the water maser emission towards S140 IRS was stronger (up to 46 Jy with at least seven features) A month after that they observed it again in January 2001, some

of maser features had diminished and the features was detected in May 1999 has disappeared. A new and single weak maser feature was detected in January 2001 and remained the only feature in the spectrum until June 2001 when a weak new feature appeared. This result shows that the water maser emission varies with time. More recently work by Trinidad et al. (2007), they detected three water masers toward IRS 1 (as shown in Figure 4.3) that most probably are tracing unbound motion and are associated with the bipolar molecular outflow in the northeast-southwest direction.

4.2 OH Masers in S140-IRS1

Out of the 4 transitions observed in the OH ground state, emission was only detected at 1665 MHz. The observations in the other OH ground-state transitions at 1612, 1667 and 1720 MHz did not reveal any signal down to a noise level of 21 mJy beam^{-1} ($3\,\sigma_{\rm rms}$) at each frequency. Earlier single-dish observations by Baudry et al. (1997) revealed very faint emission at 6035 MHz. In the current observations at 6031 MHz and 6035 MHz, no signal was detected down to an upper limit of 18 mJy beam^{-1}. Therefore, in the results and discussion presented hereafter, only OH maser emission from the 1665 MHz line will be considered.

4.2.1 Kinematics and Distribution

The OH emission detected by MERLIN towards S140-IRS1 came from two distinct regions, which have been labelled the 'upper group' and the 'lower group'. Figure 4.4 presents their spectra in the left-hand circular (LCP) and right-hand circular (RCP) polarizations as well as all the 4 Stokes parameters. The velocity range covered by the two groups is slightly different: the upper group covers a velocity range from -8.72 to $-4.58\,{\rm km\,s^{-1}}$, while the lower group covers a velocity range from -10.02 to $-5.56\,{\rm km\,s^{-1}}$. Maser emission is detected from 13 different spectral line features, six of which are seen in LCP and seven, in RCP. The results for these 13 features are summarized in Table 4.1. For each feature, the table gives the velocity, relative position, position uncertainty and the peak flux density in both hands of circular polarization. The positional uncertainties in each feature have been calculated from the standard deviation of the particular feature.

Figure 4.5 presents the spatial distribution of the 1665-MHz OH maser features relative to the reference position of the maser features given is R.A.= $22^{\rm h}19^{\rm m}\,18\overset{\rm s}{.}2180$ and Dec.= $+63^\circ\,18'\,46''.779$ (J2000). The velocity of each maser feature is also given. It can be seen that the emitting regions are very small: the upper group covers a region of 30×10 milliarcsec^2 while the lower group covers a region of 50×10 milliarcsec^2. These regions are localised on a North East - South West (NE-SW) axis, separated by approximately 1 arcsec.

Plots of R.A. offset vs. velocity and Dec. offset vs. velocity are shown in the left and right panels of Figure 4.6 respectively. Neither plots shows any systematic variation with position on the sky. Instead, one can observe two groups separated by $\sim$0.6 arcsec in R.A., and by $\sim$0.7 arcsec in Dec. The upper group has velocities

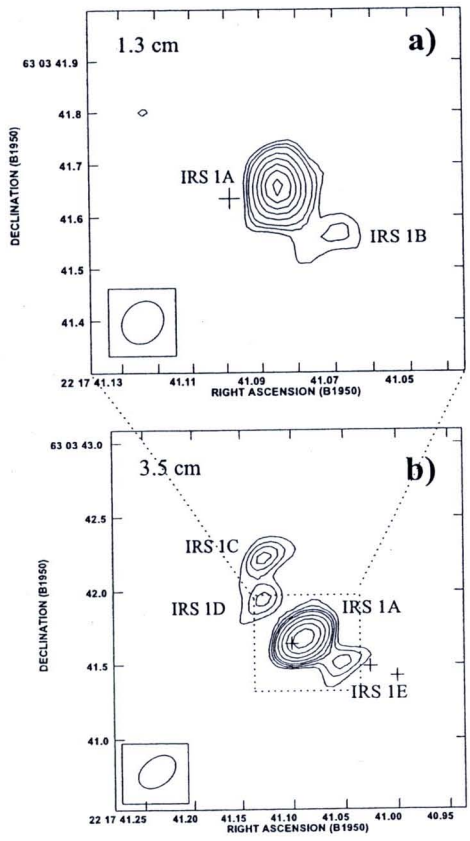

Figure 4.1 Multiple radio continuum sources detected toward S140 IRS 1A at different wavelengths. *a)* 1.3 cm continuum contour map. Contours are -3,3,4,5,7,9,11,13 and 15 times 230 μJy beam^{-1}, the rms noise of the map. The beam size is $0''.09 \times 0''.07$. *b)* 3.5 cm continuum contour map. Contours are -3,3,5,7,9,11,15,20,25 and 30 times 55 μJy beam^{-1}, the rms noise of the map. The beam size is $0''.29 \times 0''.20$. The crosses show the position of the water masers detected in the region (taken from Trinidad et al. 2007).

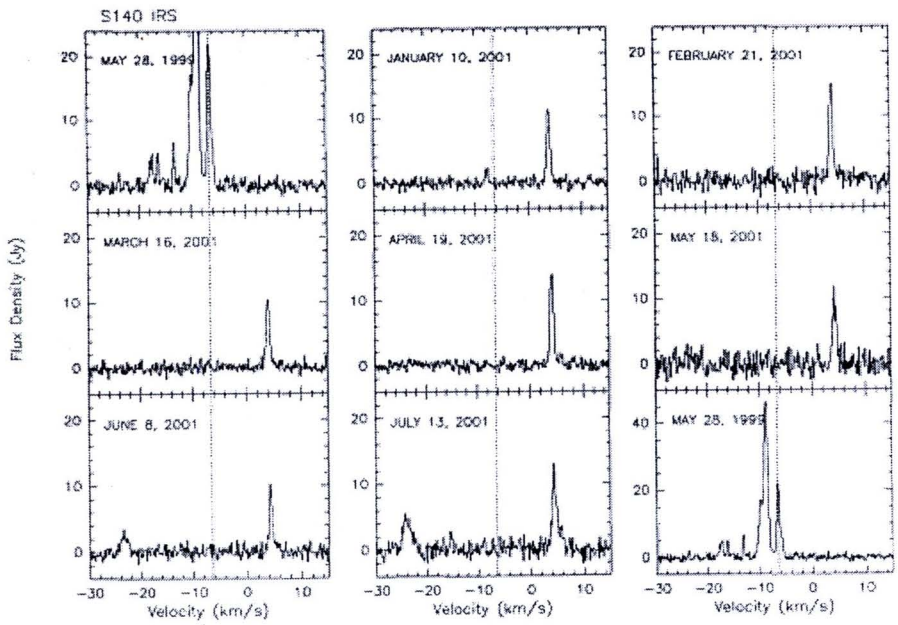

Figure 4.2 The systemic velocity of the source is -6.5 km s^{-1} (vertical dashed line). The first spectrum is repeated at the end of the sequence with a different scale for the peak flux density (taken from Trinidad et al. 2003).

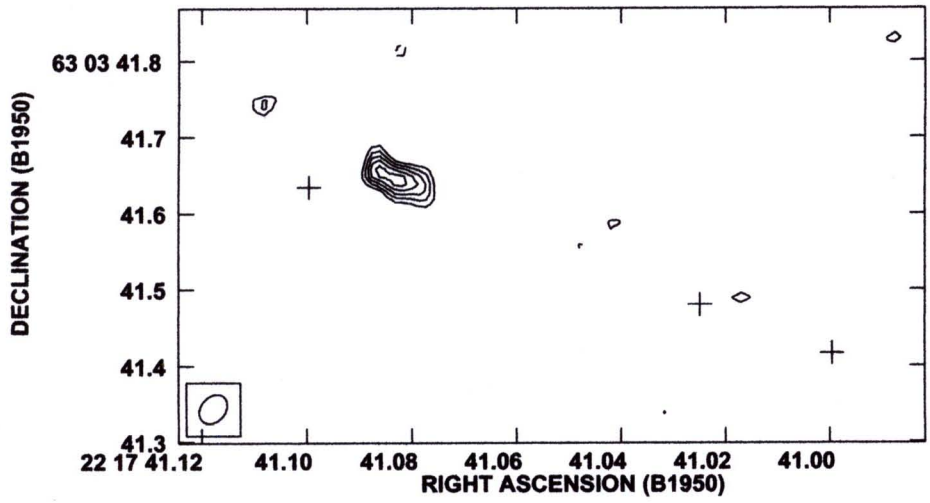

Figure 4.3 Contour map of S140 IRS 1A at 7 mm. Contours are –3,3,4,5,6 and 7 times 310 μJy beam^{-1}, the rms noise of the map. The beam size (0″.04 × 0″.03) is shown in the lower left corner. The crosses show the position of the water masers observed toward the IRS 1A (taken from Trinidad et al. 2007).

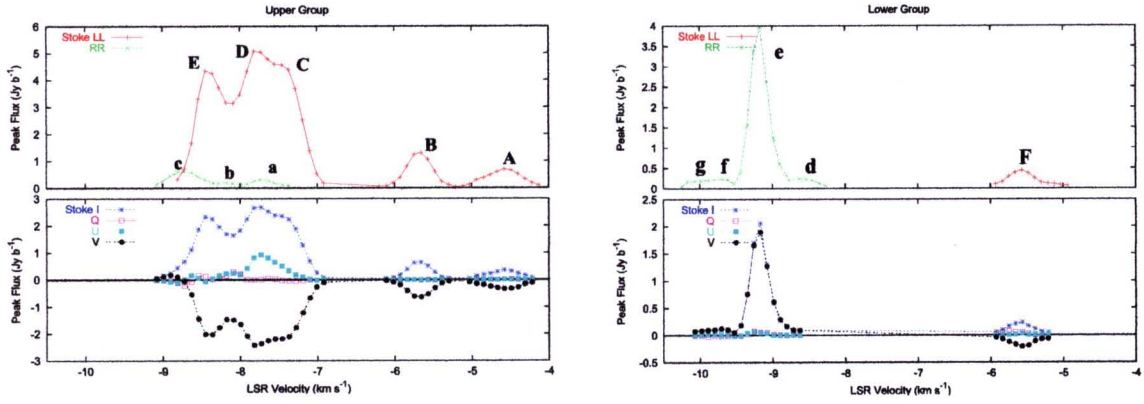

Figure 4.4 Left panel: The upper panel shows the spectra in LCP and RCP for the upper group detected by MERLIN at 1665 MHz OH towards S140-IRS1. The peak of all the spectral features identified are labelled from A to E and a to c in LCP and RCP respectively. These features are listed in Table 4.1. Bottom panel: the corresponding spectra in the I, Q, U and V Stokes parameters. The right panel shows the same as the left panel for the lower group.

Table 4.1 OH maser features in S140-IRS1. Peak flux density, mean velocities and relative positions are given for each feature in both polarizations.

Circularly polarized features	Stokes No.	Velocity[a] (km s^{-1})	R.A.Offset[b] (arcsec)	σ_{RA}[c] (arcsec)	Dec.Offset[d] (arcsec)	σ_{Dec} (arcsec)	Peak (Jy $beam^{-1}$)	Comment[e]
1665-LCP:								
Upper								
A	1	−4.58	−1.635	0.011	2.018	0.005	0.70	Z_1-**5.4** mG
B	2	−5.68	−1.614	0.009	2.018	0.006	1.31	Z_2-**5.2** mG
C	3	−7.35	−1.624	0.005	2.015	0.002	4.58	
D	4	−7.78	−1.637	0.003	2.017	0.001	5.09	
E	6	−8.38	−1.634	0.009	2.018	0.001	4.36	
Lower								
F	8	−5.56	−2.171	0.015	1.310	0.012	0.45	Z_3-**6.9** mG
1665-RCP:								
Upper								
a	4	−7.74	−1.636	0.003	2.010	0.007	0.32	Z_1
b	5	−8.16	−1.640	0.004	2.014	0.005	0.21	
c	7	−8.72	−1.618	0.010	2.012	0.004	0.69	Z_2
Lower								
d	9	−8.56	−2.208	0.006	1.310	0.003	0.23	
e	10	−9.18	−2.198	0.001	1.310	0.001	3.98	
f	11	−9.65	−2.169	0.004	1.309	0.006	0.24	Z_3
g	12	−10.02	−2.187	0.010	1.303	0.005	0.19	

[a]Velocity with respect to the local standard of rest (LSR), assuming a rest frequency of 1665.402 MHz.

[b]R.A. offset from reference position at R.A.(J2000)=$22^h19^m\ 18^s.2180$.

[c]The positional uncertainties in each feature are calculated from the standard deviation of the position of the components of each feature.

[d]Dec. offset from reference position at Dec.(J2000)=63°18′.46″.779.

[e]The number is cross-referenced to Table 4.2

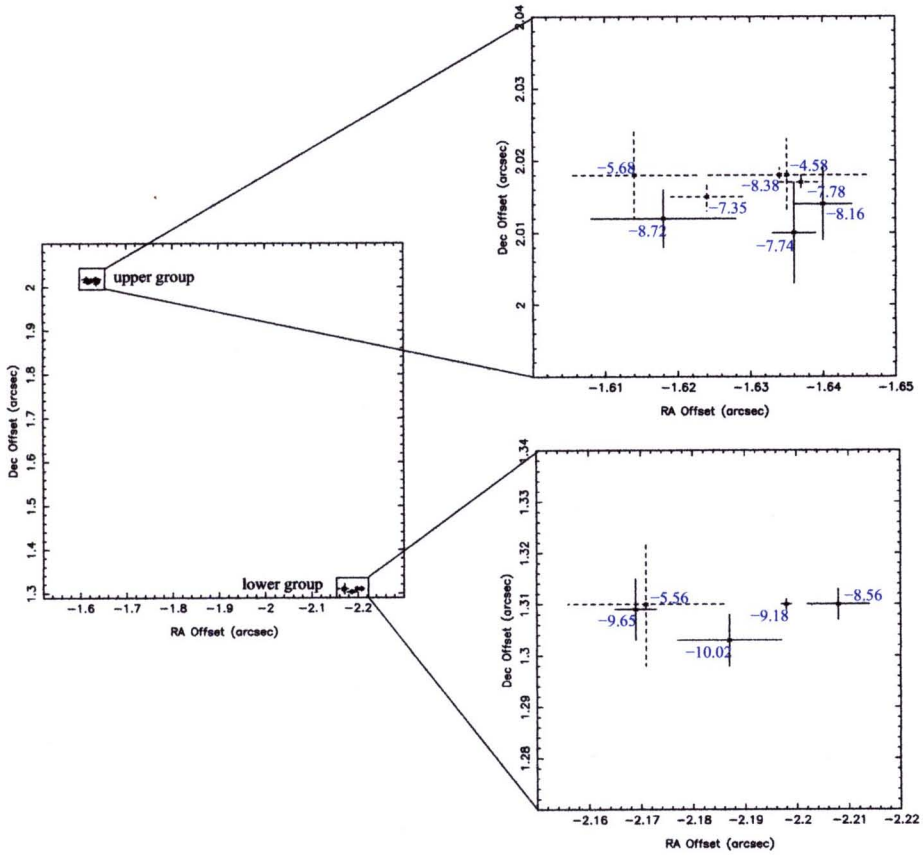

Figure 4.5 The left panel shows the maser features at 1665 MHz. They are distributed in 2 regions that we labelled to be 'upper' and 'lower' groups. The right panel shows the positions and velocities of maser components in these upper and lower groups separately. The RA and Dec offsets are relative to the reference position at R.A.(J2000)=$22^{h}19^{m}\ 18^{s}.2180$, Dec.(J2000)=63°18′46″.779. The velocity of each individual component is also given. Dashed and solid lines represent LCP and RCP respectively.

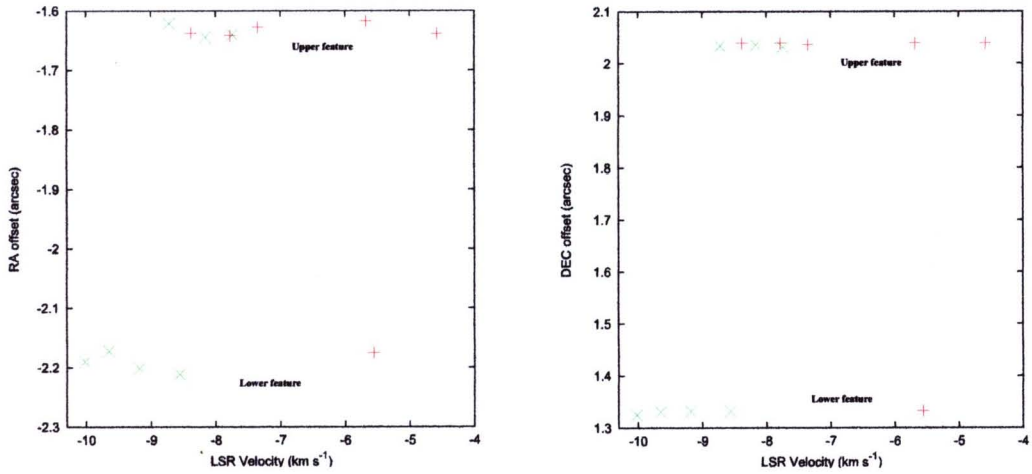

Figure 4.6 Left and right panels plot the association between velocities and positions in right ascension (RA) and declination (Dec) respectively with respect to the pointing position at R.A.(J2000)=$22^{\rm h}19^{\rm m}$ $18^{\rm s}.2180$, Dec.(J2000)=63°18′46″.779. Plus and cross symbols are 1665L and 1665R masers which are listed in Table 4.1.

ranging from –4.58 to –8.72 km s^{-1}, the lower group from –5.56 to –10.02 km s^{-1}. These seem to indicate that the maser features in this region are distributed with a velocity gradient along the line of sight.

4.2.2 Polarization and Magnetic Fields

Full polarization information for the 1665-MHz OH maser emission is given in Table 4.2, which lists the mean velocity, relative position, the Stokes I, Q, U, V peak flux densities, the linear polarized flux density (P) position angle (χ) the percentages of linear (m_L), circular (m_C) and total polarization (m_T) of each feature identified in the Stokes I data cube. The typical uncertainty in position angle is ±5°. The uncertainty in the percentage polarization is between 1 and 15 per cent. From Table 4.2, it can be seen that features 2 and 9 are purely circularly polarized and that the linearly polarized features can be divided into 2 groups, the first having the weaker linear polarization (8 per cent for features 1, 6 and 10), and the second having values of 15–30 per cent (features 3, 4, 5, 8, 11 and 12).

Figure 4.7 plots the percentage of circular polarization against the percentage of linear polarizaton for the 1665-MHz masers. The m_T values are mostly above 85 per cent with only one feature less than 35 per cent. These results agree well with the modelling of polarization characteristics at 1665 MHz by (Gray et al. (2003), cf. their figure 7). We compared our results with Gray et al. model because, it is the only coupled polarized maser and magnetohydrodynamic model which currently exists. Hutawarakorn and Cohen (2003, 2005) examined the possibility that a low degree of polarization could arise because of a blending of components that are close in position and in velocity. This could be the situation for Feature 7.

Table 4.2 The Stokes parameter flux densities and polarization properties of OH maser features in S140-IRS1.

Stoke No.	Com.[a]	Vel. (km s^{-1})	I [b] (Jy b^{-1})	Q (Jy b^{-1})	U (Jy b^{-1})	V (Jy b^{-1})	P [c] (Jy b^{-1})	χ [d] (°)	m_L [e] (%)	m_C [f] (%)	m_T [g] (%)
1665 MHz											
Upper											
1	A	−4.58	0.363	+0.020	+0.017	−0.340	0.026	+25	7.2	−93.5	93.8
2	B	−5.68	0.651	−0.004	−0.003	−0.631	0.005	–	0.8	−97.0	97.0
3	C	−7.38	2.363	−0.018	+0.510	−2.179	0.511	−1	21.6	−92.2	94.7
4	D,a	−7.75	2.693	+0.014	+0.929	−2.352	0.929	+0.4*	34.5	−87.4	93.9
5	b	−8.18	1.705	+0.166	+0.242	−1.457	0.294	+17	34.5	−87.4	93.9
6	E	−8.45	2.339	+0.136	−0.058	−2.008	0.148	+57	6.3	−85.8	86.1
7	c	−8.72	0.684	−0.202	+0.008	−0.047	0.202	−44	29.5	−6.8	30.3
Lower											
8	F	−5.57	0.239	+0.058	+0.034	−0.207	0.068	+30	28.2	−86.5	91.0
9	d	−8.63	0.098	+0.002	−0.002	+0.095	0.003	–	3.0	+101.5	101.6
10	e	−9.17	2.060	+0.060	+0.047	+1.898	0.076	+26	3.7	+92.1	92.2
11	f	−9.62	0.110	−0.012	+0.013	+0.104	0.017	–	15.6	+94.6	96.0
12	g	−9.89	0.096	−0.015	+0.017	+0.100	0.022	−21	23.1	+104.5	107.1

Notes:

1.C, D and E suffer from blending, especially C and D, the peak intensity of D is likely to be overestimated.

2.* The polarization angle of feature D is hardly affected by the blending with feature a.

[a]The component positions for both hands of circular polarization R and L given in Table 4.1 and those for the I Stokes dataset were measured independently but they agree within the position uncertainty.

[b]Peak flux intensity in Stokes I and use the position of the I peak to measure peak flux in Stokes Q, U and V.

[c]Linear Polarization Intensity, P = $(Q^2 + U^2)^{1/2}$.

[d]The polarization angles (χ) were not measured if the linearly polarized flux was less than the noise level (noise level> 3 × rms ∼21 mJy).

[e]The percentage of linear polarization of the maser line, m_L, is defined as $m_L = 100 \times (Q^2 + U^2)^{1/2}/I$.

[f]The percentage of circular polarization $m_C = 100 \times (V/I)$.

[g]The percentage of total polarization of the maser line, m_T, is defined as $m_T = 100 \times (Q^2 + U^2 + V^2)^{1/2}/I$.

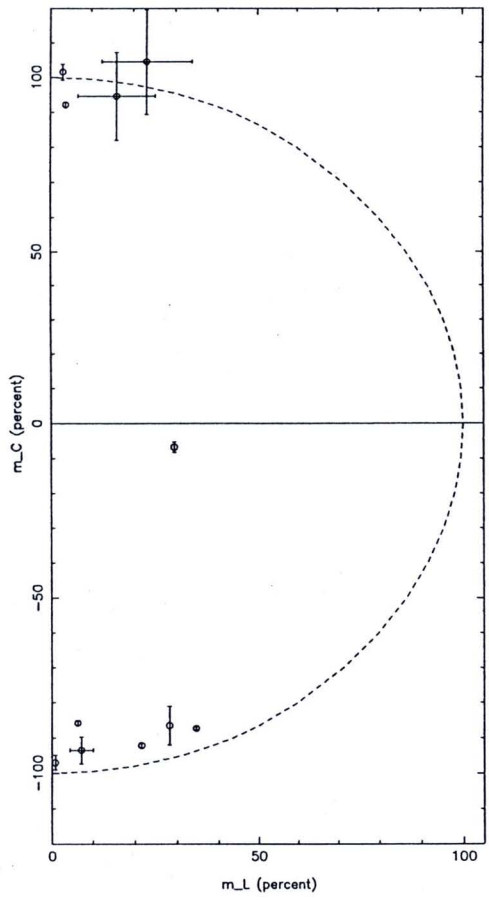

Figure 4.7 Percent of linear (m_L) versus circular (m_C) polarization of each Stokes I feature in S140-IRS1. The dotted semicircle traces the locus of a 100 per cent polarized feature, m_T=$(m_C^2$+$m_L^2)^{1/2}$. Negative values of m_C come from negative values of Stokes V.

It is possible that this feature is a blend of a σ-component (i.e., associated with feature 2 of Table 4.2, implying $\vec{B}$ perpendicular to the plane of the sky and for which a value of 5.2 mG has been calculated) and a π-component that could arise from a different OH maser spot along the line of sight with $\vec{B}$ parallel to the plane of the sky.

Figure 4.8 shows the relative positions of the features listed in Table 4.2. There are two possible Zeeman pairs in the upper group and one pair in the lower group, which indicate a magnetic field directed towards us with a strength ranging from 5.2 to 6.9 mG. Similar strengths have been found in other SFRs (e.g. in W75N: Hutawarakorn et al. 2002, in ON1 and K3-50: Fish et al. 2005). However, it has to be noted that Baudry et al. (1997) and Curran and Chrysostomou (2007) found lower values for the magnetic field strength in the region (+2.8 mG and

+0.4 mG respectively), but the Baudry et al. results come from single-dish measurements at 6035 MHz and the Curran et al. results, from infrared polarization measurements from the dust. Both of these earlier observations therefore consider much larger angular scales than the present work. The 3 Zeeman pairs, identified in the current data, could arise from different, widely separated parts of the region. However, it has also been shown from 3-D modelling of the SFR, W75N, that different values for the magnetic field can be measured in the same disc (cf. Gray et al. 2003).

Linear polarization position angles have been measured in nine elliptically polarized OH features. They have values of +25, −1, +0.4, +17, +57 and −44 degree for the upper group and +30, +26 and −21 degree for the lower group. The mean (and dispersion) for the upper group is 9° (30°), and for the lower group 11° (23°), so both groups could have the same magnetic field direction. The implications of this are discussed further in Section 4.4.2.

4.3 H_2O Maser and the Radio Continuum Emission

H_2O maser emission occurs at four locations within a one-arcmin diameter circle centred on IRS1. As the extent of this is more than half the MERLIN 22 GHz primary beam and the more distant masers were already affected by integration-time smearing, it could be that there are even more distant masers, which are not visible because of this smearing. The positions and other properties of the detected masers are given in Table 4.3. Figure 4.13 shows their relative positions and also the relative positions of the OH masers detected by us and the H_2O masers detected by Trinidad et al. (2007). The region labels are chosen simply not to conflict with other labels used or quoted in this work. H_2O masers have been detected at all epochs close to IRS1 (region Q) covering a wide velocity range (almost 30 km s^{-1}). Trinidad et al. (2007) detected three H_2O maser clumps using the VLA, all of which have nearby MERLIN counterparts at similar velocities. However, the VLA positions are offset systematically by 40–50 milliarcsec to the SW of the MERLIN positions: this could be caused by the coarser resolution of the VLA and its lower positional accuracy, especially since the emission was very weak at the time of the VLA observations (epoch 2000). The flux densities as a function of velocity are compared in Figure 4.9. The brightest emission detected by MERLIN is close to the IRS1 infra-red continuum peak, region Q: 26 Jy at 10.2 km s^{-1} in 1998 and 315 Jy at 2.9 km s^{-1} in 2004. Emission has been detected in the outlying region, P, only in 1998, and in region, S, only in 2004. Regions P and S are at distances and position angles of 29 arcsec, 300° and 6.9 arcsec, 290° respectively relative to IRS1. Emission has also been detected by MERLIN at both epochs from region R (to the south of IRS1), which is at a distance of 16.5 arcsec and position angle 240° relative to IRS1. However, this emission had become fainter and covered a smaller velocity range in 2004. Figure 4.10 shows the positions of the H_2O masers detected in 2004 near the IRS1 radio continuum. A 'chain' of masers, containing the brightest 22-GHz emission, crosses the main 5-GHz radio continuum feature near its centre. The maser chain, at a position angle

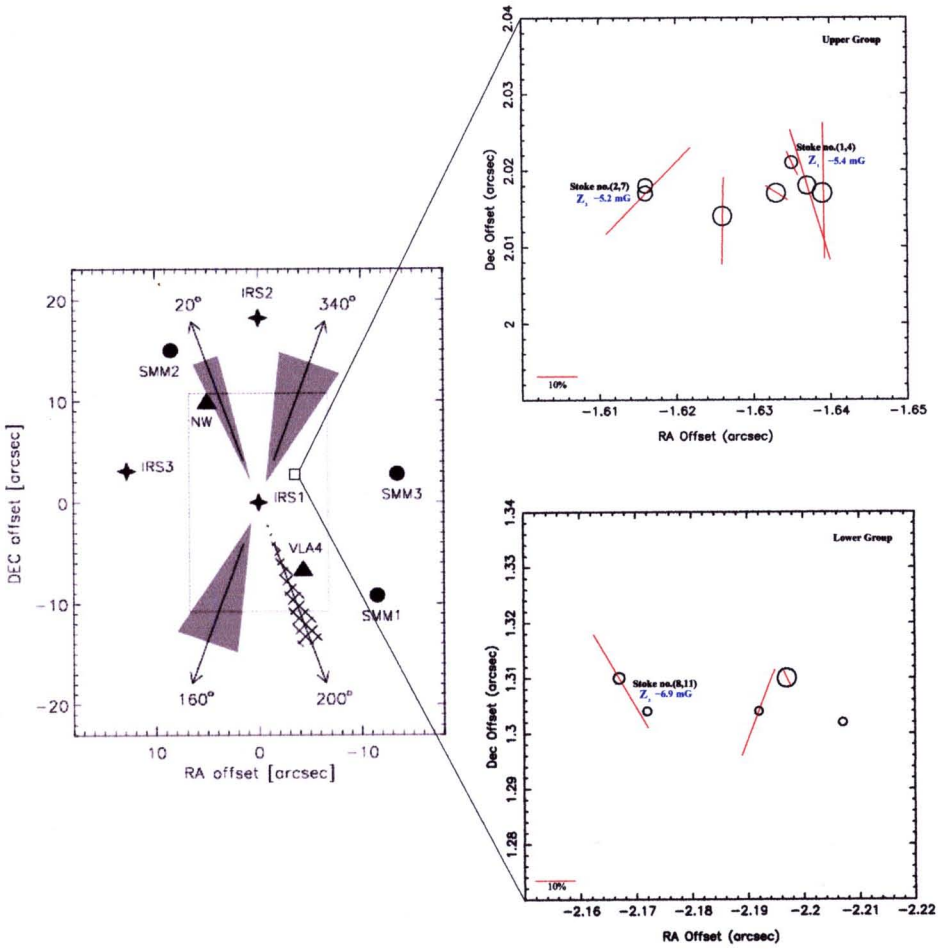

Figure 4.8 The left panel is taken from Weigelt et al. (2002); it shows a schematic map of the S140 region. The asterisks mark the positions of the infrared sources, the dots are the submm peaks and the triangles are radio continuum sources. Outflow directions are indicated by arrows superposed on shaded triangles. The right panel shows OH masers in S140 IRS1 plotted with polarization information in both components. The vectors indicate the direction of the electric field vector, and have lengths proportional to the percentage of linear polarization. The area of each circular symbol is proportional to the logarithm of the Stokes I peak flux. Numbers on the figure are the magnetic field strengths deduced from Zeeman pairs.

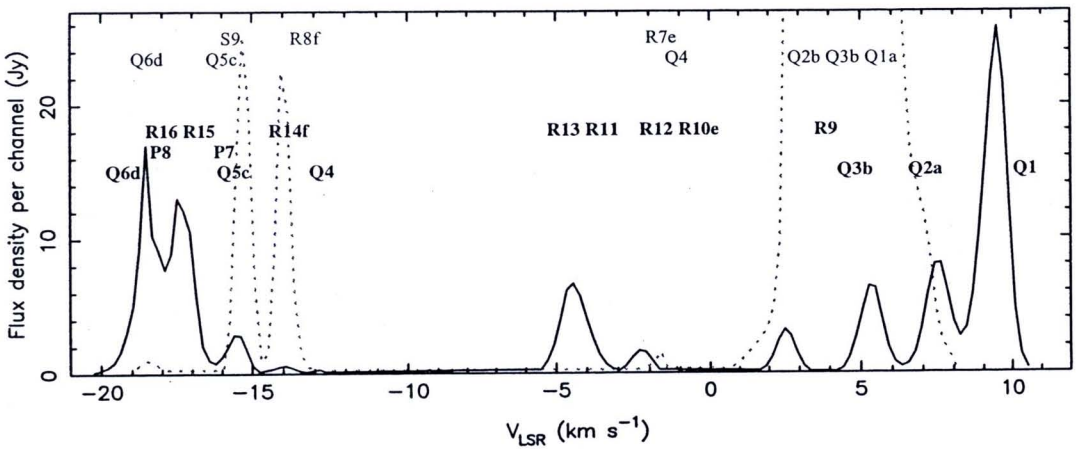

Figure 4.9 The velocity profiles of H_2O maser emission summed from images of data taken in 1998 (solid lines, bold labels) and 2004 (dashed lines, fine labels), labelled with the regions of origin listed in Table 4.3.

of 120°–130°, is almost orthogonal to the direction of elongation of the continuum. An additional maser feature lies near the outer error circle of the unresolved VLA continuum region E. The maser clumps close to IRS1 have been detected but not resolved by Trinidad et al. (2007) and Tofani et al. (1995), with similar peak velocities, but in the latter observations the outlier close to the VLA continuum region E was brightest.

4.4 Discussion

A comparison of the OH 1.7-GHz and H_2O 22-GHz maser distributions with previous images of the region is presented in Figure 4.11. Astrometric corrections to the maser positions R.A.(J2000)=$22^h19^m18^s.2180$, Dec.(J2000)=63°18′46″.779. Panel (a) shows the positions of both maser species in the S140 IRS region superimposed on a CO emission map adapted from Hayashi et al. (1987). Panel (b) shows an enlargement of the box drawn in panel (a); it shows the positions of the 1.7-GHz OH and 22-GHz H_2O masers obtained with MERLIN, and the 22-GHz H_2O masers detected with the VLA. Panel (c) is an enlargement of the small box from panel (b); the OH masers are separated from the H_2O masers by ∼2.5 arcsec in the direction of the red-shifted CO outflow, but the velocity range of the OH masers is similar to that of blue-shifted CO outflow. Panel (d) shows an enlargement of the H_2O masers within 1×1 arcsec^2 of IRS1.

4.4.1 Information from OH Maser Modelling

Using the maser modelling of Gray et al. (1992), an upper limit to the number density in the OH maser regions can be determined from the absence of maser emission at 6035 MHz. Masers at 6035 MHz require a molecular hydrogen

Table 4.3 H_2O masers observed towards S140. The group labels contain the upper-case letter label of the region as shown in Figure 4.13, the group number at that epoch and the lower-case letter identifying the matched feature at the other epoch (if any). The position etc. of each group is the weighted average for emission in a discrete region. ΔV is the V_{LSR} span of each group, x and y are the offsets from $22^h19^m18^s.2180$ $+63°\ 18'.46''.779$ J2000, L is the maximum angular extent of each group and I_{max} is the flux density of the brightest component. Proper motion measurements are given for the 2004 group of each matched pair. The less likely match is shown in italics.

Group	V_{LSR}	ΔV	x	σ_x	y	σ_y	L	σ_L	I_{max}	δ_{xy}	$\sigma_{\delta xy}$	V_{PM}[a]	σ_{VPM}[b]	θ_{PM}[c]	$\sigma_{\theta PM}$[d]
	(km s^{-1})		(mas)		(mas)		(mas)		(Jy)	(mas)		(km s^{-1})		(deg)	
1998															
Q1	10.2	2.5	122.1	0.0	247.0	0.01	0.6	1.5	25.79						
Q2a	6.6	2.3	122.4	0.0	248.0	0.03	0.9	2.9	8.05						
Q3b	4.8	3.2	107.2	0.0	265.2	0.04	5.6	8.7	6.39						
Q4	-12.8	0.8	-550.8	1.2	25.0	1.2	1.2	4.1	0.28						
Q5c	-15.5	1.5	-381.1	0.1	98.3	0.1	2.5	1.8	2.44						
Q6d	-18.1	1.3	5.0	1.3	303.6	1.5	1.2	7.4	0.19						
P7	-15.4	1.5	-25062	4	14023	4	4	14	0.78						
P8	-17.6	2.1	-25060	3	14023	3	1	14	8.22						
R9	2.7	2.1	-14229	3	-7660	3	4	14	3.21						
R10e	-2.3	1.5	-14185	4	-7592	4	4	14	1.46						
R11	-4.0	2.7	-14175	3	-7604	3	4	14	6.47						
R12	-2.4	1.3	-14209	4	-7637	4	4	14	0.58						
R13	-4.0	1.9	-14227	4	-7662	4	5	14	0.25						
R14f	-14.6	2.7	-14261	2	-7718	2	10	14	0.57						
R15	-17.1	4.8	-14264	2	-7718	2	5	14	16.74						
R16	-17.9	2.3	-14295	3	-7728	3	19	14	0.75						
2004															
Q1a	7.1	2.1	143.99	0.17	222.53	0.16	6.3	1.4	2.13	33.4	0.3	19.5	0.2	139.6	0.6
Q2b	2.9	7.4	115.05	0.01	237.20	0.01	4.2	0.5	314.9	29.1	0.1	17.0	0.1	164.3	0.2
Q3b	*3.8*	*3.6*	*78.16*	*0.01*	*256.66*	*0.01*	*13.2*	*0.5*	*310.7*	*30.3*	*0.1*	*17.7*	*0.1*	*253.6*	*0.2*
Q4	-1.3	0.8	66.14	0.47	261.75	0.55	8.0	2.2	0.52						
Q5c	-15.1	1.3	-377.44	0.01	88.05	0.01	0.6	0.2	21.29	10.9	0.2	6.4	0.2	160.3	1.3
Q6d	-18.6	1.0	33.72	0.13	291.78	0.13	9.8	1.7	0.98	31.1	2.7	18.1	1.6	112.3	5.0
R7e	-1.9	0.6	-14144.5	0.2	-7579.8	0.2	2.0	1.3	1.02	42	8	25	5	74	11
R8f	-13.2	1.7	-14293.6	0.1	-7753.0	0.1	5.4	1.4	22.54	48	6	28	3	223	7
S9	-15.3	0.8	-3991.5	0.3	1917.2	0.1	0.8	0.3	5.44						

[a]The proper motion velocity
[b]The proper motion velocity uncertainty
[c]The proper motion position angle
[d]The proper motion position angle uncertainty

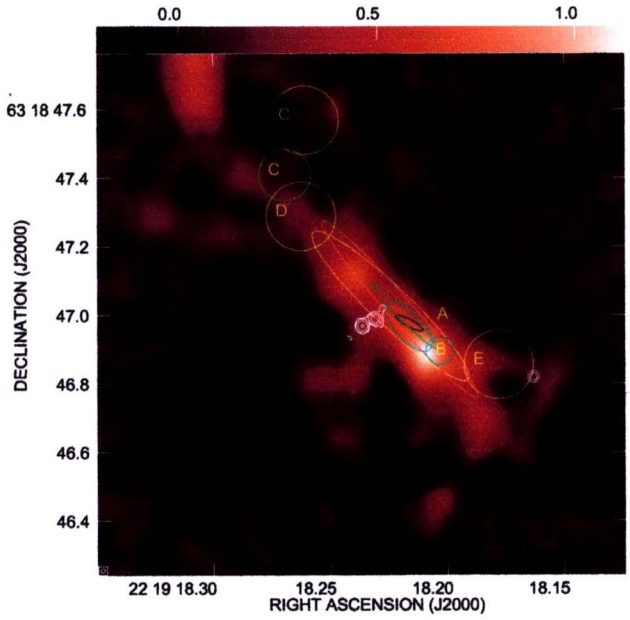

Figure 4.10 The 'flame' scale shows 5-GHz continuum emission observed in 2000 using MERLIN and re-imaged as mentioned in Chapter 3 Section 3.3.4. The white contours show the H_2O masers in this region. The masers overlying the radio continuum correspond to 2004 Q1,2,3,4,6 (Table 4.3) with a velocity gradient from -19 to $7\,\mathrm{km\,s^{-1}}$ from NW to SE. The outlying emission to the west is 2004 Q5, at $-15\,\mathrm{km\,s^{-1}}$. The ellipses show the continuum emission reported and labelled as in Trinidad et al. (2007); blue, cyan, green, yellow and red represent 0.7, 1.3, 2, 3.5 and 6-cm data, respectively, observed using the VLA.

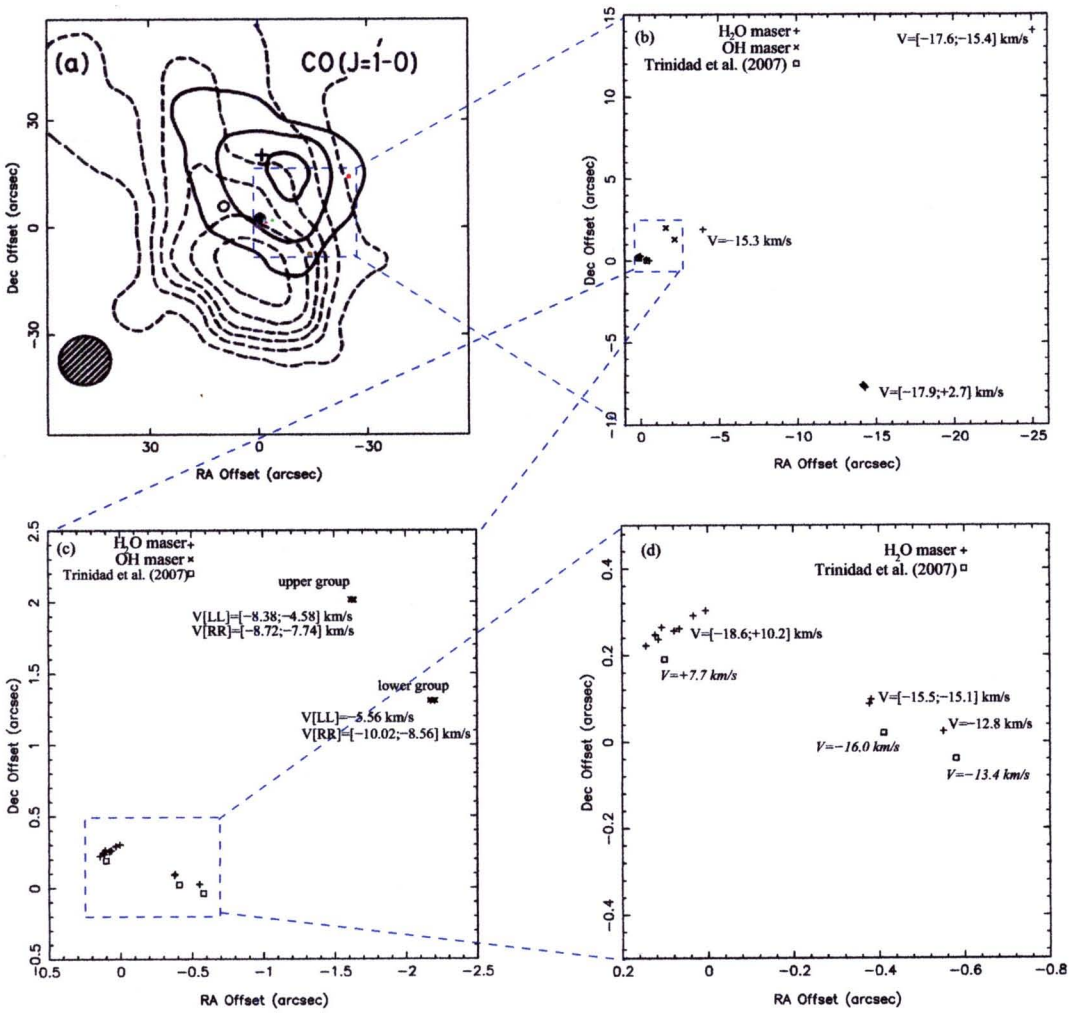

Figure 4.11 Panel (a) shows OH and H_2O masers are superimposed on the CO emission map adapted from Hayashi et al. (1987). The dashed and solid contours are the blue (-30 and $-12\,\mathrm{km\,s^{-1}}$) and red (-3 to $+10\,\mathrm{km\,s^{-1}}$) wings. Symbols represent various sources as follows, filled circle: IRS1, cross: IRS2, open circle: IRS3. Panel (b) is a blow up of the box drawn in panel (a); it shows the positions of our 1.7 GHz OH and 22 GHz H_2O masers, obtained with MERLIN, and the 22 GHz H_2O masers detected with the VLA towards the S140 IRS region. The velocity of each maser component is indicated. Panel (c) is a blow up of the small box from panel (b). It shows the positions of both maser species in a box of size 3.0×3.0 arcsec^2. Panel (d) shows the position of our MERLIN H_2O masers (plus symbols) and those previously detected by Trinidad et al. (2007) (rectangular symbols).

density (n_{H_2}) of at least $2\times10^7\,cm^{-3}$. Therefore, it is reasonable to assume that the number density in the S140 OH maser regions is substantially lower than this, and is most likely to be in the optimum range for strong 1665 MHz maser emission, between 10^6 and $2 \times 10^6\,cm^{-3}$. Alternatively, the constraint can be viewed in terms of the number density of OH (n_{OH}), where the 1665-MHz emission tends to come from regions with n_{OH} >15-20 cm^{-3}, but 6035-MHz emission requires at least $100\,cm^{-3}$ of OH. Models also impose a weaker constraint on the kinetic temperature (T_K) in the maser region, with temperatures below 75 K favouring 1665-MHz masers, whereas 6035-MHz emission requires 75-150 K.

The energy density of the masing gas, calculated from the modelled values of n_{H_2} and T_K is $\varepsilon = 6.9 \times 10^{-10} n_6 T_{50}\,Jm^{-3}$, where n_6 is the H_2 number density in multiples of 10^6 cm^{-3} and T_{50} is the kinetic temperature in multiples of 50 K. This value can be compared with the energy density, $B^2/(2\mu_0)$, in the observed magnetic field, which can be written as ε_B=$9.95\times10^{-8}B_5^2$ Jm^{-3}, where B_5 is the observed magnetic field in multiples of 5 mG. Thus, in the OH maser region of S140, the magnetic energy density is two orders of magnitude larger than the value expected for equipartition of energy, which suggests that the magnetic field dominates the dynamics. The strength of the magnetic field favours the ambipolar diffusion theory of cloud collapse to form pre-stellar cores over the supersonic turbulence theory, since the presence of a magnetic field is far more important in the former theory.

4.4.2 Kinematics of the OH Masers

The OH maser velocities show no systematic variation with position on the sky. As there are only a few spots of maser emission, and these cover a small area, it is possible that only a small part of the cloud is being seen. Moreover, it seems that the brightest H_2O masers originate from the direction of the disc associated with the 5-GHz continuum source. Since the OH masers are separated from the H_2O masers by approximately 2.5 arcsec in the NW direction (cf. Figure 4.11) it appears that both species trace different material within the star forming region.

There are three plausible hypotheses for the OH maser spatial distribution observed: **1)** the OH masers originate from a separate disc associated with S140, but not with IRS1; **2)** the OH masers are probing the upper rim of the CO outflow from IRS1; **3)** the OH masers are associated with the H_2 outflow from IRS1.

1. In the first hypothesis, the separation between the OH masers and the H_2O masers being ~2.5 arcsec, implies that the OH masers would originate from a separate disc which is significantly shifted away from the centre of IRS1. This object would have to be in a very early stage of evolution, as there is no associated continuum emission from an HII region.

The lack of systematic position-velocity gradient in the OH masers makes a disc interpretation uncertain. If it is the case, the mass derived from a Keplerian analysis of a disc, based on the approximation of a point-like and dominant central mass is given by,

$$\frac{M_*}{M_\odot} = 0.561 \frac{d_{\rm kpc}\theta'' v^2_{\rm obs,k}}{\cos^2\phi}, \tag{4.1}$$

where $d_{\rm kpc}$ is the distance to the source in kpc, θ'' is the separation of the two OH maser regions in arcseconds, $v_{\rm obs,k}$ is half the observed velocity separation of the maser regions, measured in km s^{-1}, and ϕ is the inclination angle of the disc to the line of sight, with $\phi = 0$ being the edge-on condition. The velocity separation is based on the flux-weighted mean velocities of all the maser features in each region. For the S140 OH masers, values of $d_{\rm kpc} = 0.764$, $\theta'' = 1.04$ and $v_{\rm obs,k} = 0.66$, give a central mass of $M_*/M_\odot = 0.194/\cos^2\phi$. For any reasonable value of ϕ (close to zero) this mass is much too small to be a ZAMS B-type star. As the OH masers trace a disc which is independent of IRS1, there is no requirement for it to be a B-star, but an estimate of a minimum mass can be made on the grounds that this object actually supports OH masers. The most similar objects to the above are Class II methanol masers enclosing protostars with a lower mass limit of $\leq 3\,{\rm M}_\odot$ (Minier et al., 2003). If it is assumed that this limit also applies to OH masers, with which the Class II methanol variety is closely associated in many sources, then an estimate can be made of the size of the protostellar disc required to enclose this minimum mass. For a Mestel disc, with an assumption of no central condensation and therefore a better description of an unevolved object, it is possible to show that the mass enclosed within a radius, r, is $M(r) = rv_{\rm c}^2/G$, where $v_{\rm c}$ is the circular speed, which is independent of radius. If $v_{\rm obs} = v_{\rm c}\cos\phi$, then the disc radius required to contain a mass $M(r)$ is,

$$r = 890 \left(\frac{M(r)}{M_\odot}\right) \frac{\cos^2\phi}{v^2_{\rm obs,k}} {\rm AU}, \tag{4.2}$$

noting that the masers need not be at the edge of such a disc. For $M(r) = 3\,M_\odot$, eq.(4.2) gives a radius, r, equal to $6140\cos^2\phi\,{\rm AU}$, which is a plausible value for a very young protostellar object, still containing a substantial mass in the disc as opposed to a centrally condensed protostar.

2. In the second hypothesis, the OH masers are associated with the CO outflow from IRS1 in the 340° direction. The two maser regions could be on opposite sides of an approximately conical outflow and correspond to the near and far sides of the 340° wing of the outflow. This hypothesis is supported by Jiang et al. (2008) who observed several massive young stellar objects in K-band polarimetric images. In the case of S140-IRS1, the polarized disc delineates the edge of the disc, and the 5-GHz continuum emission, detected by Hoare (2006), traces an ionized equatorial disk wind, which is strongly related to the CO outflow. The magnetic field vectors derived from the linear polarization measurements of the OH masers, have a mean orientation of $(10 \pm 30)°$, see Fig. 4.8 and Section 4.2.2. This could be aligned with the eastern side of the CO outflow if it has even a modest opening angle.

3. Observations by Preibisch and Smith (2002) indicate the presence of multiple outflows in the S140-IRS1 region. However, the position of the origin of these H_2 outflows is uncertain by approximately 1.2-1.6 arcsec, and may not

coincide with the centre of IRS1. It is therefore possible that the H_2 outflow, orientated along an axis in the 20°/200° direction, could be associated with the OH maser region, noting that the maser region lies ~2″.5 to the NW of IRS1. In this scenario, the upper OH feature would be associated with the NE lobe of the H_2 outflow, and the lower one, with the SW lobe. The OH maser magnetic field vectors could also be consistent with this orientation.

Based on our observations, the most likely scenario of the above three hypotheses is considered to be either the first or the second.

4.4.3 Kinematics of the H_2O masers

The 2004 and 1998 data have been compared to match component groups, assumed to be the same if their centroids are within 50 milliarcsec and velocity differences within 2.0 km s^{-1}. Increasing the limits to 100 milliarcsec and 3 km s^{-1} respectively produced more multiple matches but no unique additional matches. Matched groups are marked in Table 4.3 and the components are plotted in Figure 4.12. The detailed similarities of the component distributions of the matched features, and the systematic displacements of all 3 features in region Q suggest strongly that the same clumps of gas have been identified. The shifts in velocity are less than the total velocity spans of some features, but the position shifts of the feature centroids, δ_{xy}, are two or more times greater than the angular extent of the features. Six features detected in 2004 had counterparts in 1998. The 1998 and 2004 observations were separated by 2273 days, and adopting a distance of 764 ± 27 pc, proper motion velocities, $V_{\rm PM}$, have been calculated and marked with arrows in Fig. 4.12.

In region Q (Figure 4.13 and Table 4.3), three matched pairs at the position of IRS1 (a, b, d) have $29 < \delta_{xy} < 34$ milliarcsec between 1998 and 2004, all in a similar direction, at proper motion position angles, $\theta_{\rm PM}$, of 110°–165°. The only ambiguous match (to b) has $\theta_{\rm PM} = 254°$, so, unless the motions are highly disordered, this seems less likely. The position shifts correspond to $17 < V_{\rm PM} < 20$ km s^{-1} in a SE direction. The matched groups cover a wide velocity range (−19 to 10 km s^{-1}), increasing systematically from NW to SE over ~160 milliarcsec. The fourth pair of matched groups, (c), is offset ~500 milliarcsec to the SW, with a similar $\theta_{\rm PM}$ and a smaller δ_{xy}, corresponding to $V_{\rm PM} = 6.4$ km s^{-1}.

There are two matched groups in region R (e, f) with $\theta_{\rm PM}$ of $74 \pm 11°$ and $223 \pm 7°$ respectively in almost completely opposite directions, suggesting expansion proper motion at $25 < V_{\rm PM} < 28$ km s^{-1}, away from a common origin between the features.

Although there is a possible uncertainty of up to 25 milliarcsec in comparing data at different epochs, the different, but systematic proper motions in the two regions suggest that the alignment is very accurate. The maximum uncertainty gives a possible proper motion range of 2–43 km s^{-1} directed between south and east for the main part of region Q, but the outlying clump, (c), could be moving in any direction. The maximum alignment uncertainty would make the outflow velocities in group R less symmetric and add a bulk shift in any direction. The

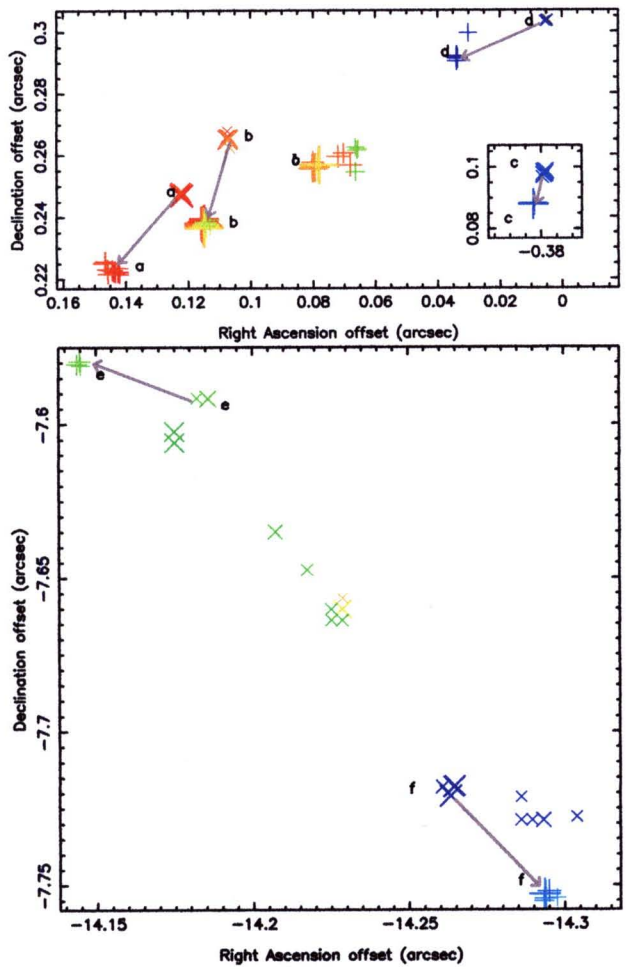

Figure 4.12 H_2O maser components in the regions Q (left panel) and R (right panel) where proper motions were identified. 1998 and 2004 data are represented by × and + symbols, respectively. The matched groups are labelled with their identifying letters as in Table 4.3. The shading represents velocity, blue being blue-shifted and red being red-shifted with respect to the midpoint of $-5\,\mathrm{km\,s^{-1}}$. The size of the symbols is proportional to the logarithm of the component flux density. (0, 0) is at $22^{\mathrm{h}}19^{\mathrm{m}}\ 18^{\mathrm{s}}.2180\ +63°\ 18'\ 46''.779$ (J2000). The arrows indicate the proper motions of some water masers.

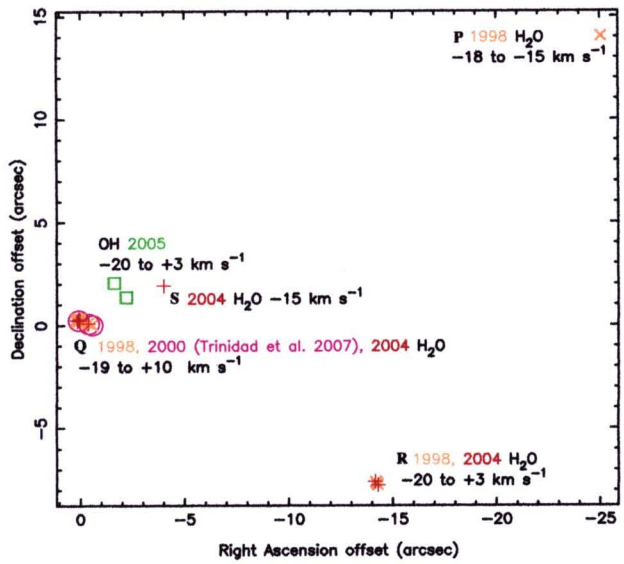

Figure 4.13 The relative positions of H_2O and OH masers detected at the epochs indicated. The continuum emission from IRS1 is located in region H. The maximum velocity range covered at each location is indicated. (0, 0) is at $22^h19^m\ 18^s.2180$, $+63°\ 18'\ 46''.779$ (J2000).

uncertainty in the distance is ~ 3 per cent, which does not affect the proper motion directions.

There are no published bulk proper motion measurements for S140, but the open cluster Pismis-Moreno 1, less than 5 arcmin away and at the same distance, has a proper motion of < 1 milliarcsec yr^{-1} (Dias et al., 2002), so this is unlikely to be an issue, although peculiar motions of individual YSOs are possible.

The ordered velocity gradient and proper motions of the central group (a, b and d) in region Q could be interpreted either as a rotating disc or as an outflow. The $V_{\rm LSR}$ changes by 29 km s^{-1} over 0.16 arcsec. If these features were part of a disc in Keplerian rotation, the maximum proper motion velocity gives the rotational velocity $v_{\rm rot} \approx 20$ km s^{-1} (or a lower limit if we do not detect the part of the disc where the motion is in the plane of the sky). The line of sight velocity at the limbs of the disc is $v_{\rm obs,k} = 14.5$ km s^{-1} (as defined in Section 4.4.2). The angle of inclination of the disc is given by $\phi \geq \arccos(v_{\rm obs,k}/v_{\rm rot})$. Equation 4.1 then gives $M_* \leq 22\,M_\odot$. However, if this were the case, a greater range of proper motion velocities would be expected, with lower values nearer the limbs. This is not so, as all three values are similar.

4.4.4 The Relationship Between the Water Masers and the Other Sources in S140

Long-term single-dish monitoring of the H_2O masers by Lekht et al. (1993) shows that the water masers are extremely variable. They interpret the triple-peaked profile and fluctuations as indicative of emission from a Keplerian disc. Our

images show that the spectrum contains contributions from components which are too widely spatially separated to originate from a single disc. However, such an interpretation cannot be ruled out for individual regions, such as Q, which does possess a triplet spectrum.

The radio continuum emission has been interpreted both as a disc wind (Hoare, 2006) or associated with jets (e.g. Preibisch et al., 2002), which would require multiple jets, since the radio continuum emission is orthogonal to the CO outflow. The conflicting evidence is reviewed by Trinidad et al. 2007. The H_2O maser region Q is elongated perpendicular to the radio continuum longest axis, which is only compatible with a disc interpretation of both phenomena if is more than one source in IRS1, as suggested by Weigelt et al. (2002).

The direction of elongation and proper motions of the masers at Q is similar to the CO outflow (Hayashi et al., 1987). The masers are being pushed in the SE direction at a transverse velocity of $\sim 18\,\mathrm{km\,s^{-1}}$ (with $\sim 14\,\mathrm{km\,s^{-1}}$ and 45° uncertainty if our alignment of epochs is inaccurate). However, the CO outflow is blue-shifted ($-30 < V_{\mathrm{LSR}} < -12\,\mathrm{km\,s^{-1}}$) to the SE and red-shifted ($-3 < V_{\mathrm{LSR}} < 10\,\mathrm{km\,s^{-1}}$) to the NE, whereas the H_2O maser velocity gradient across IRS1 is in the opposite sense. If the H_2O masers are associated with the outflow, they represent a region $\sim 150\,\mathrm{AU}$ wide, and of unknown depth, which is expanding both away from and towards us along the line of sight. Cooling, post-shock gas is known to favour H_2O masers (Elitzur et al., 1992), so it is feasible that a strong outflow from IRS1 is causing shocks to propagate with a wide opening angle and large-scale turbulence.

The outlying maser clump of region Q, close to the IRS1 continuum feature, E, (Figure 4.10), is also moving more slowly towards the SE. This suggests that it is material swept away by the disc wind (Hoare, 2006) and is not associated with the outflow suggested by Weigelt et al. (2002) at a position angle of 200°. However, the maximum alignment uncertainty would allow motion in the outflow direction.

The maximum separation of almost half an arcminute between IRS1 and water maser group P corresponds to a light-travel time of up to 5 months at the distance of S140, but a wind or jet with a velocity of only several hundred $\mathrm{km\,s^{-1}}$ would take several centuries to pass between the regions. If the spectral variations between regions P, Q, R and S (and possibly other regions at other epochs) are correlated, this must be because of changes in the luminosity of a common exciting source, not a shock wave. Lekht et al. (1993) describe long-term anti-correlated fluctuations of the maser peaks on a timescale of approximately a year, caused by competition in maser pumping. It seems improbable, given the high optical depths in the region, that illumination could penetrate from IRS1 to P, even if this mechanism were to be applicable within region Q. Maser variability could also occur as a result of extreme amplification, which might occur if one cloud passes in front of another (Kartje et al., 1999). Variability would also be expected in masers emanating from post-shocked gas perpendicular to the shocked direction (Elitzur et al., 1992).

The compact, apparently bipolar, outflow of H_2O masers in region R is just

under 4 arcsec from SMM1, one of three sub-millimetre sources in the region detected by Minchin et al. (1995). Their observations had a pointing accuracy better than 3 arcsec, but they measured a source extension greater than 10 arcsec, so it is possible that these masers are located in outflows from the protostar postulated by Minchin et al. (1995), which is close to an NH_3 peak (Zhou et al. 1993). This region is not aligned with any other outflow so far detected so it could be powered by an independent, very young or low-mass source.

Regions P and S have no obvious continuum counterparts and are at a position angle 290°–300°; region R is at a position angle of 240°, all with respect to IRS1. In both cases these are significantly offset from the nearest outflow directions deduced by Weigelt et al. (2002) at 340° and 200° respectively, requiring jets with opening angles of 80°. This would represent a width >0.15 pc at 29 arcsec separation from region P, which seems unlikely. Moreover, the H_2O masers in these regions are all blue-shifted, apart from the slightly red-shifted wing in R, but the CO and H_2 outflows in these directions are red-shifted. It is more probable that they are caused by other exciting sources in this complex region.

The OH masers are located 2.5 arcsec NW of IRS1 and the main H_2O maser clump, Q, at position angles of 295° and 315°. This corresponds to a separation of approximately 1900 AU. The separation between the OH masers and region S is similar. There is no obvious association, apart from proximity to the 340° CO outflow (770–1400 AU from its axis at the distance of the OH masers). OH masers generally trace cooler, lower-density, less violent conditions than H_2O masers.

4.5 Summary

The new high-sensitivity data show that the OH masers in S140 are in two distinct groups separated by ~1 arcsec. Both groups have similar velocity patterns, and the overall number of spots is small. Consequently, there is no clear evidence for disc structure but such a possibility is not ruled out. The magnetic field, deduced from measurements of Zeeman splitting, is uniform in its direction (towards us), with values ranging from −5.2 to −6.9 mG. These values are large enough for the magnetic field to play a significant role in the dynamics of the maser region. The polarization results show strong circular polarization of the OH masers, generally above 80 per cent. The fractional linear polarization is weaker than the fractional circular polarization in all but one feature. The direction of the magnetic field and the location of the OH maser regions indicate that they may be associated with the CO outflow from S140-IRS1. Alternatively, the OH masers may trace a disc around a hitherto undetected protostellar object.

The strongest water masers are associated with IRS1 and have a bulk proper motion towards the SE. However, their Doppler velocities are red-shifted, whereas the CO outflow is blue-shifted in this direction. A separate pair of masers, 15 arcsec to the WSW, appear to be expanding away from a common centre. Additional water maser components appear up to 30 arcsec from IRS1 with no obvious counterparts or alignments with any of the known outflows in the region. The OH and water maser results suggest that there are multiple excitation sources. Another

set of interferometric observations is needed to disentangle between the scenarios proposed here.